Research Square

Preprints are preliminary reports that have not undergone peer review.
They should not be considered conclusive, used to inform clinical practice,
or referenced by the media as validated information.

Integrated Valorisation of Spartium junceum into a Bioactive Cellulose Acetate/Halloysite Nanofibrous Wound Dressing with Sustained Antioxidant Availability and Enhanced Fibroblast Migration

Özlem Yılmaz Karaboyacı

okaraboyaci@pau.edu.tr

Pamukkale University

Semra Kılıç

Süleyman Demirel University

Research Article

Keywords: Spartium junceum, cellulose acetate, halloysite nanotubes, electrospinning, fibroblast migration, biomass valorisation

Posted Date: November 2nd, 2026

DOI: https://doi.org/10.21203/rs.3.rs-10821671/v1

License: This work is licensed under a Creative Commons Attribution 4.0 International License.
Read Full License

Additional Declarations: No competing interests reported.

Integrated Valorisation of *Spartium junceum* into a Bioactive Cellulose Acetate/Halloysite Nanofibrous Wound Dressing with Sustained Antioxidant Availability and Enhanced Fibroblast Migration

Özlem Yılmaz Karaboyacı and Semra Kılıç*

Ö. Yılmaz Karaboyacı: Pamukkale University, Acıpayam Vocational School, Textile, Clothing, Footwear and Leather Department, Footwear Design and Production Program, 20160 Denizli, Türkiye

Corresponding author: okaraboyaci@pau.edu.tr

ORCID: Özlem Yılmaz Karaboyacı https://orcid.org/0000-0002-2936-871X

S. Kılıç: Süleyman Demirel University, Department of Biology, Faculty of Engineering and Natural Sciences, 32260 Isparta, Türkiye

ORCID: Semra Kılıç https://orcid.org/0000-0001-9494-2952

Keywords: *Spartium junceum*; cellulose acetate; halloysite nanotubes; electrospinning; fibroblast migration; biomass valorisation

Abstract

An integrated cascade-valorisation strategy was developed to convert *Spartium junceum* (Spanish broom) flower biomass into a cellulose acetate/halloysite nanotube (CA/HNT) nanofibrous wound-dressing platform. Volatile constituents were first recovered by steam distillation, and the residual aqueous phase was then partitioned sequentially with hexane and chloroform; the exhausted lignocellulosic biomass was subsequently converted to cellulose and then to cellulose acetate. The synthesised cellulose acetate had a degree of substitution of 2.66 ± 0.04 (n = 3). GC–MS identified chemically distinct major constituents in each fraction, with linoleic acid methyl ester (51.02%) dominant in the hexane fraction and 1,4-benzenedicarboxylic acid dimethyl ester (29.37%) and palmitic acid methyl ester (25.10%) dominant in the chloroform fraction. A 12% (w/v) CA formulation containing 3 wt% extract-loaded HNT produced homogeneous, bead-free nanofibers with diameters of approximately 130–200 nm (mean ≈173 nm, measured from SEM micrographs). FTIR, XRD, and DSC confirmed successful acetylation and formation of the composite nanofibrous matrix. The dressing showed balanced water-management behaviour, was non-cytotoxic to L929 fibroblasts by ISO 10993-5, and increased scratch closure to 97.2% at 48 h versus 64.8% for untreated controls. CUPRAC measurements showed antioxidant activity in the release medium for up to 48 h, peaking at 0.055 mM Trolox equivalents at 2 h. Together, these findings demonstrate the feasibility of coupling renewable cellulose-acetate production with phytochemical recovery and nanofiber fabrication in a single biomass-valorisation platform.

1. Introduction

Acute and chronic wounds are difficult to manage when inflammation, oxidative stress, microbial burden, and impaired cell migration disrupt normal tissue repair. Advanced wound dressings are therefore expected to do more than cover the wound: they should maintain a moist environment, support gas exchange and exudate management, and provide a biologically compatible interface for tissue repair (Boateng et al. 2008; Dhivya et al. 2015; Jangde et al. 2018; Junker et al. 2013).

Electrospinning is well suited to this purpose because it produces highly porous, fibrous membranes with large specific surface area and tunable fiber diameter. Electrospun scaffolds provide an extracellular-matrix-like surface architecture and can simultaneously serve as carriers for therapeutic or naturally derived compounds (Li and Xia 2004; Pham et al. 2006; Xue et al. 2017, 2019).

Cellulose acetate (CA) is an attractive electrospinning matrix because it combines the renewable origin of cellulose with good solution processability and an established record in membrane and biomedical-material applications. Its properties are strongly influenced by the degree of substitution (DS), which governs solubility, polarity, chain packing, and thermal behaviour, making DS a key parameter linking cellulose derivatisation to nanofiber processing and end-use performance (Candido and Gonçalves 2016; Edgar et al. 2001; Rodrigues Filho et al. 2008).

Halloysite nanotubes (HNTs) offer an additional route to functionalise CA fibers. Their tubular aluminosilicate structure and internal lumen can retain molecular cargo, while their hydroxylated surfaces allow physical interaction with polymer matrices; HNTs have accordingly been investigated as carriers for sustained delivery and as fillers in biomedical composite systems (Fakhrullin and Lvov 2016; Lvov et al. 2016; Prinz Setter and Segal 2020; Satish et al. 2019).

Plant-derived extracts can further extend the functionality of electrospun wound dressings, although biological claims for complex extracts require caution: activity cannot generally be assigned to a single GC–MS constituent without compound-specific testing. Even so, plant-derived antioxidant and wound-repair systems demonstrate that naturally occurring phytochemical mixtures can be incorporated into biomaterial platforms while retaining biologically relevant activity, including cellulose-acetate nanofiber carriers loaded with crude plant extracts (Affonso et al. 2016; Dos Santos et al. 2021; Liu et al. 2024).

From a sustainability perspective, the same biomass can potentially serve both as a source of extractable compounds and as a lignocellulosic feedstock. Cascade valorisation, in which higher-value fractions are recovered before the structural carbohydrate fraction is converted, is consistent with circular-bioeconomy approaches for reducing the underutilisation of lignocellulosic resources (Cansado et al. 2025; Martins Vilas-Boas et al. 2025; Mujtaba et al. 2023).

Spartium junceum L. (Spanish broom) is a Mediterranean lignocellulosic species already investigated as a source of natural fibres and cellulose-derived materials (Angelini et al. 2000; Karaboyaci and Kılıç 2022; Katović et al. 2011; Kovačević et al. 2021). Its flowers also contain extractable secondary metabolites, and previous studies report biological activity or antioxidant capacity in *S. junceum*-derived fractions (Cerchiara et al. 2012; Nanni et al. 2018; Zahreddine et al. 2021). These two attributes make the species particularly well suited to an integrated, materials-oriented valorisation strategy.

Previous work has generally treated these opportunities separately: *S. junceum* has been studied either as a source of phytochemicals and fibres or as a feedstock for cellulose acetate, while CA-based wound dressings and HNT-based delivery systems have largely been developed from independently sourced components. To our knowledge, no study has combined recovery of extractable fractions with conversion of the residual *S. junceum* biomass into CA for an electrospun, HNT-containing wound dressing.

The present study therefore tests the hypothesis that sequential recovery of extractable *S. junceum* fractions can be coupled with production of highly substituted cellulose acetate from the residual biomass to yield a functional electrospun wound-dressing platform. The study integrates GC–MS profiling, DS determination, electrospinning optimisation, FTIR, XRD, DSC, water-management measurements, L929 cytocompatibility testing, a fibroblast scratch assay, and CUPRAC analysis of release media, with particular emphasis on linking biomass-derived cellulose chemistry and nanofiber structure to the measured physicochemical and *in vitro* biological performance.

2. Materials and methods

2.1. Plant material, distillation, and extraction

During the spring flowering season, 25 kg of fresh *S. junceum* flowers were collected from Direkli village, Isparta, Türkiye. Flowers were shade-dried for approximately 7 days and ground. A 300 g portion of dried flowers was steam-distilled in a Clevenger apparatus with 3500 mL water for 8 h, giving a volatile fraction yield of 0.57 g kg−1 dry flowers. The residual aqueous phase was extracted sequentially with hexane and chloroform (250 mL each). Solvent fractions were evaporated and analysed by GC–MS (Agilent 5975C/7890A; DB-WAX capillary column, 50 m × 0.20 mm i.d., 0.20 µm film) after methyl-ester derivatisation with 1.5 M methanolic HCl at 80 °C for 2 h. The GC oven program was: 80 °C (hold 4 min); ramped at 13 °C min−1 to 175 °C (hold 7 min); ramped at 4 °C min−1 to 215 °C (hold 5 min); ramped at 4 °C min−1 to 240 °C (hold 15 min). Injector and detector temperatures were both 240 °C, and the injection volume was 1 µL. Compound identification used NIST library matching. Only the major constituents of each fraction — those identified with the highest confidence and contributing most to the total peak area — are reported in Tables 1–3; numerous additional minor and trace-level peaks were also detected but are not listed individually.

2.2. Cellulose isolation and cellulose acetate synthesis

Cellulose was isolated from the exhausted *S. junceum* flower biomass by the Kurschner–Hoffer method (Kürschner and Hoffer 1931). Cellulose acetate was prepared following established acetylation procedures (Djuned et al. 2014; Rodrigues Filho et al. 2008; Cerqueira et al. 2007) and the authors' previous *S. junceum* protocol (Karaboyaci and Kılıç 2022). Briefly, 1 g cellulose was activated in 25 mL acetic acid for 1 h; 0.1 mL H2SO4 and 30 mL acetic anhydride were then added and the mixture was stirred at 22 °C for 4 h. The product was precipitated with 500 mL water, washed to pH 7, and dried at 105 °C.

2.3. Degree of substitution

Degree of substitution was determined by ASTM D871 back-titration. Dried CA (approximately 1.0 g, W) was dissolved in 150 mL DMSO, 30.0 mL of 1 N NaOH was added, and the mixture was stirred for 2 h for saponification. Excess NaOH was back-titrated with 1 N HCl using phenolphthalein. Acetyl content and DS were calculated using Eqs. 1 and 2.

$$\text{Acetyl Content (\%)} = [(V^{b} - V_s) \times N \times 0.04305 / W] \times 100 \quad (1)$$

$$DS = 3.86 \times \text{Acetyl Content (\%)} / [102.4 - \text{Acetyl Content (\%)}] \quad (2)$$

2.4. Halloysite loading

Commercial halloysite nanotubes (HNTs; reported pore volume approximately 1.25 mL g^{-1}) were loaded with a 1:1 (v/v) mixture of the distillation-derived solid lipophilic fraction and the chloroform extract. A total of 3 mL of the combined bioactive mixture was added per 2 g HNT. The suspension was ultrasonicated until visible foaming ceased and then mixed for a further 45 min to promote filling of the HNT lumen. The loaded HNTs were recovered by filtration and dried at room temperature. For electrospinning trials, extract-loaded HNT was incorporated at 1, 3, and 6 wt% relative to the dry mass of cellulose acetate; 3 wt% was selected because it gave the most stable electrospinning behaviour and the most homogeneous fibrous morphology.

2.5. Electrospinning

Cellulose acetate solutions in DMSO were screened over the 5–15% (w/v) concentration range; representative 6, 8, 10, and 12% formulations were evaluated by SEM. The optimised formulation contained 12% (w/v) CA and 3 wt% extract-loaded HNT relative to the dry CA mass. The solution was magnetically stirred for 1 h at room temperature and electrospun from a 5 mL syringe fitted with a 0.66 mm internal-diameter needle. A voltage of 2.2 kV was applied, the needle-to-collector distance was 12 cm, and the flow rate was 0.4–0.6 mL h−1. Electrospinning was performed at room temperature (approximately **20 °C**) and approximately 40% relative humidity. These conditions were selected after screening lower CA concentrations and needle-to-collector distances of 10–15 cm, both of which produced dripping or incomplete solvent evaporation.

2.6. Physicochemical characterization

Nanofiber morphology was examined by scanning electron microscopy (SEM); representative micrographs were acquired at 10 kV accelerating voltage in low-vacuum mode (≈59 Pa) at a working distance of ≈11.7 mm. Fiber diameters were measured directly from SEM micrographs using ImageJ software, with measurements taken at multiple random positions across each fiber mat; values are reported as the observed range and mean. FTIR spectra of cellulose and cellulose acetate were recorded using a JASCO FT/IR-4700 spectrometer in ATR mode over 4000–400 cm−1. XRD measurements were performed at room temperature using a Bruker D8 ADVANCE Twin-Twin diffractometer with Cu Kα radiation (λ = 1.5405 Å), operated at 40 kV and 40 mA, over 2θ = 8–80° with a 0.01° step size. DSC measurements were performed using a PerkinElmer DSC 400.

2.7. Water-management measurements

Water retention and moisture retention were determined gravimetrically. Water-vapour transmission rate (WVTR) was measured according to ASTM E96-90 Procedure D at 35 °C using MgCl2, and calculated as WVTR (g m−2 day−1) = [Δm/(t × S)] × 24, where Δm is mass change, t is time, and S is exposed membrane area.

2.8. Cell culture, cytocompatibility, and scratch assay

L929 mouse fibroblasts were maintained in DMEM supplemented with 10% FBS and 1% penicillin/streptomycin at 37 °C and 5% CO2. For subculturing, cells were detached with 0.25% trypsin-EDTA, collected in fresh medium, and centrifuged at 2000 rpm for 5 min; cell density in the resulting suspension was determined by Trypan Blue exclusion using a Thoma haemocytometer. Cytocompatibility was evaluated by MTT according to ISO 10993-5: cells were seeded at 2 × 10^3 cells per well in 96-well plates and allowed to attach for 24 h before exposure to nanofiber-extract concentrations of 0.78–50 µg mL−1 for 24–72 h (n = 3). At each endpoint, spent medium was replaced with 100 µL fresh medium containing 10 µL MTT solution (5 mg mL−1) per well; after 4 h incubation at 37 °C, the resulting formazan crystals were dissolved in 50 µL DMSO and absorbance was measured at 590 nm using a microplate spectrophotometer (Epoch, BioTek). Viability was calculated as the percentage absorbance relative to the untreated control. For the scratch assay, cells were seeded at 3 × 10^4 cells per well in 6-well plates and grown to a confluent monolayer; a linear scratch was created using a 200 µL pipette tip, detached cells were removed by washing with PBS, and fresh medium containing the 50 µg mL−1 condition was applied for 24 h before being replaced with untreated medium for the remainder of the assay. Cells were imaged at 0, 24, and 48 h, and scratch areas were quantified using ImageJ (n = 3).

2.9. Antioxidant capacity of release media

Dressing specimens (1 × 1 cm) were incubated in PBS (pH 7.4) at 37 °C and 100 rpm. Independent specimens were analysed at 0.5, 1, 2, 3, 4, 8, 12, 24, and 48 h. Total antioxidant capacity was measured by the CUPRAC method using the Cu(II)–neocuproine system and absorbance at 450 nm (Apak et al. 2004). Results are expressed as mM Trolox equivalents (n = 3 per time point). Because separate specimens rather than cumulative aliquots were used, the assay is described as time-dependent antioxidant availability rather than cumulative release kinetics.

2.10. Statistical analysis

Unless otherwise stated, quantitative data are reported as mean ± standard deviation (SD) from n = 3 independent replicates. The difference in residual scratch area between treated and untreated cultures at the 48 h endpoint was evaluated using a two-tailed Student's t-test, performed in GraphPad Prism (version 9), with $p < 0.05$ considered statistically significant; the corresponding 24 h difference is reported descriptively and was not formally tested. No other pairwise statistical comparisons were performed in this study.

3. Results and Discussion

3.1. Chemical Composition of *Spartium junceum* Extracts

GC–MS analysis showed that sequential processing generated chemically distinct volatile, hexane, and chloroform fractions (Tables 1–3). As noted in Section 2.1, Tables 1–3 list only the major constituents identified in each fraction; the summed relative abundance of the listed components was 95.1% (hexane), 94.4% (chloroform), and 95.0% (volatile fraction), with the balance attributable to minor and trace-level peaks that were detected but not individually resolved. Because fatty acids were derivatised as methyl esters prior to GC–MS, the reported ester peaks primarily describe the corresponding fatty-acid pool; biological activities documented for free fatty acids should not be assumed to apply quantitatively to their methyl esters without direct testing. The principal value of the sequential extraction lies in demonstrating recovery of chemically complementary fractions ahead of cellulose isolation.

Table 1 GC–MS-identified major constituents of the hexane extract of *Spartium junceum*

Compound	Composition (%)
Tetradecanoic acid methyl ester	3.40
Palmitic acid methyl ester	10.43
Stearic acid methyl ester	10.30
Oleic acid methyl ester	16.50
Linoleic acid methyl ester	51.02
Linolenic acid methyl ester	3.43

The hexane fraction (Table 1) was dominated by linoleic acid methyl ester (51.02%), followed by oleic (16.50%), palmitic (10.43%), and stearic acid methyl esters (10.30%), confirming efficient enrichment of lipophilic, fatty-acid-derived constituents. The corresponding free fatty acids linoleic and oleic acid have documented antibacterial activity (Dilika et al. 2000), and linoleic acid has also been implicated in cutaneous repair in experimental and review literature (Cardoso et al. 2004; Silva et al. 2018). These reports support the biological relevance of a fatty-acid-rich fraction but do not establish that the individual methyl esters identified here were responsible for the biological responses of the finished material.

Palmitic acid methyl ester accounted for 10.43% of the hexane fraction; the corresponding free fatty acid has been reviewed for antimicrobial effects (Johnson and Abugri 2014), providing further context for the extract's composition. Antimicrobial activity was not measured directly in this study, so these GC–MS data are interpreted as compositional evidence rather than proof of antimicrobial efficacy.

Collectively, the hexane profile identifies a concentrated, fatty-acid-derived fraction suitable for incorporation into the HNT-containing CA system. This fraction was selected for its high abundance of lipophilic constituents and its chemical complementarity to the other recovered fractions, not because any single GC–MS peak was assumed to determine wound-healing activity.

Table 2 GC–MS-identified major constituents of the chloroform extract of *Spartium junceum*

Compound	Composition (%)
Tetradecanoic acid methyl ester	3.99
Palmitic acid methyl ester	25.10
1,4-Benzenedicarboxylic acid, dimethyl ester	29.37
Stearic acid methyl ester	7.60
Oleic acid methyl ester	4.99
Linoleic acid methyl ester	2.14
Linolenic acid methyl ester	5.52
Eicosanoic acid, methyl ester	0.37
Oxiraneoctanoic acid, 3-octyl-, methyl ester, cis	15.29

In contrast to the hexane extract, the chloroform fraction (Table 2) showed a broader chemical profile, recovering aromatic ester, fatty-acid methyl ester, and epoxy-fatty-acid-derived constituents in addition to compounds already present in the hexane fraction. Previous work on *S. junceum* using solvents of different polarity likewise found that solvent choice changes both the classes of metabolites recovered and the resulting antioxidant response (Zahreddine et al. 2021), supporting the use of sequential extraction to broaden the range of compounds recovered before cellulose isolation.

The chloroform fraction was dominated by 1,4-benzenedicarboxylic acid dimethyl ester (29.37%), palmitic acid methyl ester (25.10%), and cis-oxiraneoctanoic acid, 3-octyl-, methyl ester (15.29%). The present reference set does not provide sufficient compound-specific evidence to assign wound-healing or antimicrobial functions to the aromatic ester or the epoxy ester detected here, and no such mechanism is inferred.

The relatively high palmitic acid methyl ester content provides continuity with the fatty-acid-rich hexane fraction, whereas the aromatic and epoxy-ester signals chemically distinguish the chloroform fraction. This complementarity supports the rationale for sequential extraction, although confirming the biological contribution of each chloroform constituent would require direct activity testing or targeted chemical isolation.

Overall, the hexane and chloroform fractions are compositionally distinct extracts obtained during cascade utilisation of the flower biomass. Their recovery increases the number of potentially valuable fractions obtained ahead of cellulose production, though the GC–MS data alone do not establish a synergistic or multi-target therapeutic mechanism.

Table 3 GC–MS-identified major constituents of the distillation (volatile) fraction of *Spartium junceum*

Compound	Composition (%)
Tetradecanoic acid, methyl ester	71.79
Pentadecanoic acid, 14-methyl-, methyl ester	3.71

Compound	Composition (%)
Palmitic acid methyl ester	1.04
Palmitoleic acid methyl ester	1.96
Stearic acid methyl ester	7.40
Oleic acid methyl ester	5.07
Linolenic acid methyl ester	4.00

In the volatile fraction (Table 3), tetradecanoic acid methyl ester was the predominant detected component (71.79%), followed by stearic (7.40%), oleic (5.07%), and α-linolenic acid methyl esters (4.00%), a pentadecanoic acid derivative (3.71%), and palmitoleic (1.96%) and palmitic acid methyl esters (1.04%). The corresponding parent compound, myristic acid, has been investigated for antitumour activity (Nishikawa et al. 1976), but this evidence is not wound-specific and cannot be extrapolated directly to its methyl ester. The low volatile-fraction yield (0.57 g kg−1 dry flowers) nonetheless confirms that steam distillation recovers a chemically identifiable fraction ahead of downstream solvent extraction and cellulose isolation.

From a process perspective, the modest volatile yield reinforces the value of cascade processing: relying on the volatile fraction alone would underutilise the biomass, whereas sequential extraction followed by cellulose recovery allows several product streams to be obtained from the same feedstock.

Table 4 summarises only the biological relevance directly supported by the cited literature for the corresponding parent fatty acids. It is provided as contextual information and should not be read as evidence that the methyl-ester derivatives detected by GC–MS reproduce those activities in the present dressing.

Table 4 Literature-supported biological relevance of selected parent fatty acids corresponding to GC–MS-detected derivatives. Activities were not directly tested for the individual methyl esters in this study

Compound identified via corresponding fatty-acid derivative	Literature-supported relevance of the parent fatty acid
Myristic acid (C14:0)	Antitumour activity reported in a mouse solid-tumour model (Nishikawa et al. 1976); not wound-specific.
Oleic acid (C18:1)	Antibacterial activity reported for isolated oleic acid (Dilika et al. 2000).
Linoleic acid (C18:2)	Antibacterial activity and wound-repair relevance reported for linoleic acid (Dilika et al. 2000; Silva et al. 2018; Cardoso et al. 2004).
Palmitic acid (C16:0)	Antimicrobial effects reviewed for palmitic acid (Johnson and Abugri 2014).

Compound identified via corresponding fatty-acid derivative	Literature-supported relevance of the parent fatty acid
Palmitoleic acid / α-linolenic acid	Detected by GC–MS; no wound-specific activity is assigned here from the present reference set.
1,4-Benzenedicarboxylic acid dimethyl ester / epoxy ester	Detected by GC–MS; no wound-healing or antimicrobial activity is assigned here from the present reference set.

The compositional data provide a chemical rationale for selecting the recovered extract for material fabrication; the biological performance of the finished CA/HNT dressing is evaluated independently in the cytocompatibility, migration, and antioxidant-capacity experiments below.

3.2. Degree of Substitution of Synthesised Cellulose Acetate

The cellulose acetate produced from residual *S. junceum* biomass had a DS of 2.66 ± 0.04 (mean ± SD, n = 3; CV = 1.6%) by ASTM D871 back-titration (Table 5), corresponding to an acetyl content of 44.1 ± 0.5%. This value falls within the range expected for highly substituted cellulose acetate and is numerically higher than values reported for several other lignocellulosic feedstocks — including sugarcane bagasse, rice husk, and oil-palm-derived cellulose — in the cited studies (Das et al. 2014; Djuned et al. 2014; Rodrigues Filho et al. 2008). As those values were obtained in independent studies under different reaction and analytical conditions, the comparison is descriptive rather than statistical. The measured DS nonetheless confirms extensive acetylation and is consistent with the observed solubility and electrospinning behaviour of the polymer (Edgar et al. 2001; Karaboyaci and Kılıç 2022).

Table 5 Degree of substitution (DS) and acetyl content of cellulose acetate from *Spartium junceum* (ASTM D871, n = 3)

Replicate	DS	Acetyl Content (%)
1	2.67	44.2
2	2.61	43.5
3	2.69	44.5
Mean ± SD	2.66 ± 0.04	44.1 ± 0.5

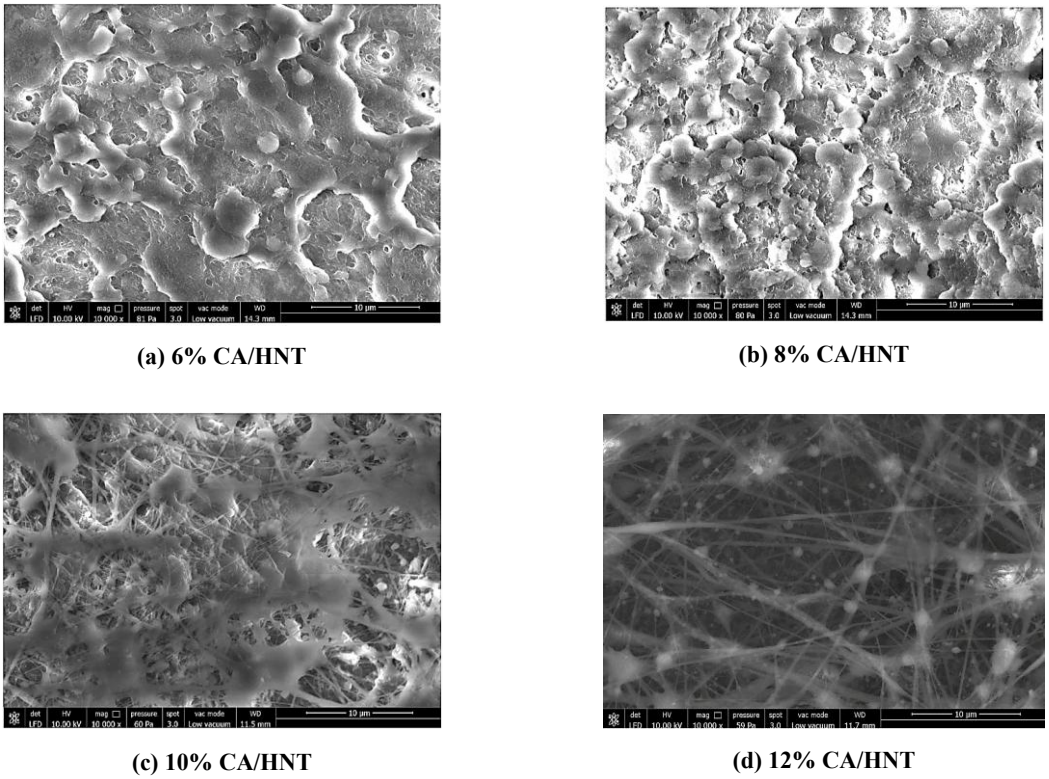
3.3. Nanofiber Morphology and Electrospinning Optimisation

SEM images showed a concentration-dependent transition from poorly defined deposits to continuous fibers (Fig. 1). At 6% and 8% CA, dripping and extensive aggregation indicated insufficient solution viscoelasticity for stable fiber formation; increasing CA concentration improved fiber continuity, consistent with the established role of polymer concentration and chain entanglement in electrospinning (Haider et al. 2018; Xue et al. 2019).

Among the formulations examined, 12% CA containing 3 wt% extract-loaded HNT produced the most homogeneous, bead-free fibrous morphology, with no visible dripping under the selected operating conditions (Fig. 1d), consistent with improved jet stability at higher polymer concentration. No large HNT agglomerates were visible at the imaging scale used, although SEM alone cannot confirm complete nanoscale dispersion of the clay within individual fibers.

Fiber diameters, measured from SEM micrographs using ImageJ (Section 2.6), ranged from approximately 130 to 200 nm with a mean of approximately 173 nm. This nanoscale morphology provides a high surface area and fibrous topography relevant to wound-contact materials and falls within the size range commonly reported for electrospun tissue-engineering scaffolds (Li and Xia 2004; Pham et al. 2006; Xue et al. 2019).

On the basis of SEM morphology and electrospinning stability, the 12% CA/3% HNT formulation was selected for subsequent physicochemical and biological measurements.



(a) 6% CA/HNT **(b) 8% CA/HNT**

(c) 10% CA/HNT **(d) 12% CA/HNT**

Fig. 1 SEM images of CA/HNT nanofibers prepared from (a) 6%, (b) 8%, (c) 10%, and (d) 12% (w/v) CA solutions containing 3 wt% extract-loaded HNT (10,000×; scale bar = 10 μm). The 12% formulation showed the most homogeneous fibrous morphology among the conditions displayed

3.4. Physicochemical Characterisation

FTIR spectra (Fig. 2) supported successful acetylation of *S. junceum* cellulose. Bands at 1748 cm−1 (ester C=O stretching), 1384 cm−1 (C–H deformation associated with acetyl groups), and 1240 cm−1 (ester C–O stretching) match characteristic cellulose-acetate absorptions and previous analysis of CA prepared from the same biomass (Karaboyaci and Kılıç 2022); the strong carbonyl signal is consistent with the high DS measured by titration.

The CA/HNT nanofiber spectrum retained the principal CA bands and additionally showed features attributable to halloysite near 904, 601, and 475 cm−1 (Satish et al. 2019). The carbonyl band shifted slightly from 1748 to 1739 cm−1 after composite formation, consistent with a change in the local interaction environment — possibly hydrogen-bonding or other interfacial interactions between CA and HNT — although FTIR alone cannot establish a unique interaction mechanism.

No new dominant absorption bands indicative of new covalent functionality appeared after electrospinning, supporting physical incorporation of HNT within the CA matrix while the characteristic chemical structure of cellulose acetate was retained.

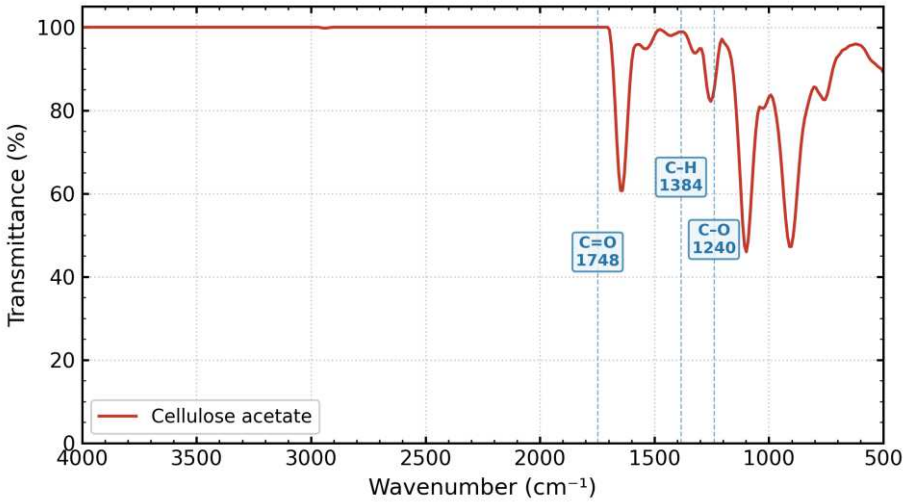


Fig. 2 FTIR spectrum of cellulose acetate from *Spartium junceum* cellulose confirming C=O (1748 cm^{-1}), C–H (1384 cm^{-1}), and C–O (1240 cm^{-1}) bands

XRD analysis (Fig. 3) showed the broad diffraction features expected for highly substituted cellulose acetate, including features near 2θ ≈ 9° and 14° together with a broad amorphous contribution at higher angles. These observations are consistent with disruption of the native cellulose hydrogen-bonding and packing arrangement during acetylation, giving a cellulose-acetate structure containing both ordered and disordered domains (Candido and Gonçalves 2016; Chen et al. 2016; Edgar et al. 2001). Peak positions are reported descriptively, following the general conventions recommended for cellulosic diffraction patterns (French 2014), rather than as indexed Miller planes: the low crystallinity and broad, overlapping reflections of this highly substituted, amorphous-rich CA precluded reliable indexing, and a crystallinity index or full-pattern deconvolution was not attempted.

The broad halo between approximately 18° and 23° indicates a substantial disordered contribution. Substitution of hydroxyl groups by acetyl groups is expected to alter chain packing and reduce the ordered hydrogen-bonding network of native cellulose (Candido and Gonçalves 2016; Edgar et al. 2001); accordingly, the XRD data are used here to describe structural change qualitatively rather than to claim a quantitative degree of crystallinity.

Because Fig. 3 represents the cellulose-acetate sample alone, no HNT-specific phase assignment is made from this pattern. Confirming HNT crystallinity within the composite would require an XRD trace of the CA/HNT material and, ideally, a companion pattern for neat HNT acquired under the same conditions. Overall, the XRD results complement the FTIR and DSC measurements, showing that acetylation substantially altered cellulose packing while measurable structural order was retained in the resulting CA.

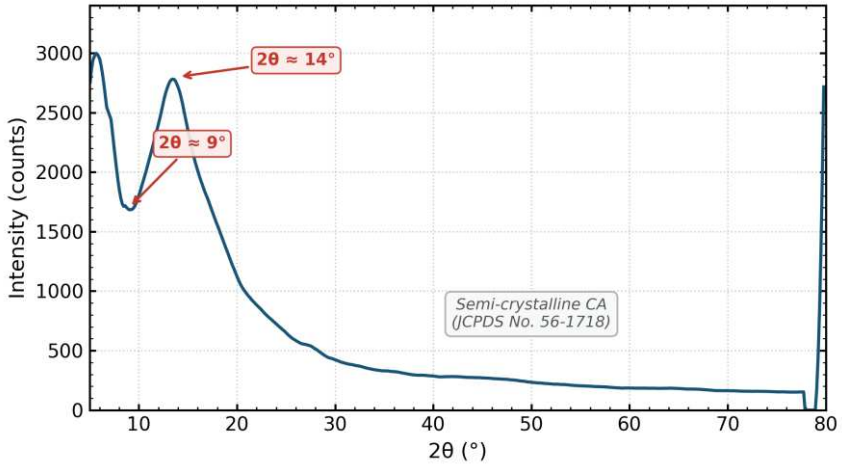


Fig. 3 XRD pattern of cellulose acetate produced from *Spartium junceum* cellulose. The pattern is interpreted qualitatively; no crystallinity index was calculated

DSC analysis (Fig. 4) showed an initial endothermic event near 74 °C, attributed to loss of residual moisture and/or physically retained solvent, and a higher-temperature transition near 191 °C. This thermal profile is broadly consistent with highly substituted cellulose acetate, although assigning an exact glass-transition temperature from DSC can be influenced by residual solvent, thermal history, and baseline selection (Edgar et al. 2001; Karaboyaci and Kılıç 2022).

The feature near 191 °C is therefore reported as an apparent glass-transition region rather than an independent measure of DS, and is interpreted alongside the chemically determined DS, FTIR, and XRD results.

A broad high-temperature endothermic event occurred between approximately 276 and 301 °C, with a maximum near 294 °C. Because cellulose acetate can undergo overlapping thermal softening, melting-like transitions, and degradation at elevated temperature, this event should not be assigned unambiguously to melting without complementary thermogravimetric analysis (TGA); the present data describe the observed thermal-transition profile but do not, on their own, establish decomposition temperature or long-term thermal stability.

Taken together, DS, FTIR, XRD, and DSC provide mutually consistent evidence that *S. junceum* cellulose was successfully converted to a highly substituted cellulose acetate that could be processed into electrospun fibers under the conditions used here.

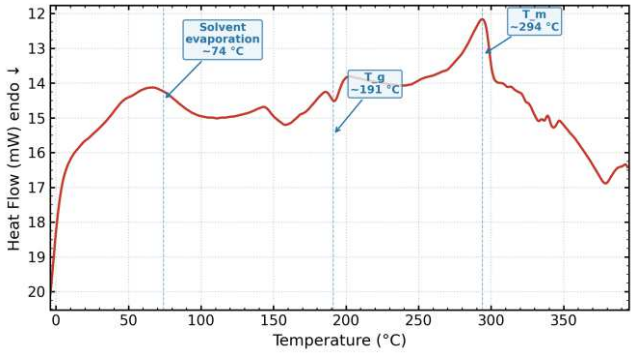


Fig. 4 DSC thermogram of cellulose acetate produced from *Spartium junceum* cellulose. High-temperature events are interpreted cautiously because complementary TGA was not performed

3.5. Physical Performance

Water retention (Fig. 5) increased from 42% at 0.5 h to approximately 54% between 1.5 and 2.5 h, then decreased to 46% at 3.5 h. This time-dependent profile indicates rapid water uptake followed by partial loss or redistribution of retained water, compatible with the porous fibrous morphology and the coexistence of relatively hydrophobic CA with hydrophilic HNT surfaces; the individual contributions of these components were not separated experimentally.

Moisture retention (Fig. 6) reached a maximum of 4.848% at 3 h and declined to 3.030% by 15 h. Because maintenance of a moist environment is widely recognised as beneficial to wound repair (Boateng et al. 2008; Jones et al. 2006; Junker et al. 2013), and a dressing should avoid both excessive desiccation and prolonged fluid accumulation, these data indicate measurable short-term moisture retention; direct comparison with commercial dressings would require testing under matched conditions.

WVTR was time-dependent (Fig. 7), with transient values of approximately 2000–2500 g m−2 day−1 during the early measurement interval and an overall mean of 1458 g m−2 day−1 across the experiment. Because literature target values for wound dressings vary with wound type, exudate level, temperature, humidity, and test configuration (Boateng et al. 2008; Jones et al. 2006), the early transient values are not interpreted as proof of a universally optimal clinical window; rather, the membrane clearly permits appreciable water-vapour transport while retaining some moisture, which is the relevant functional balance for further evaluation.

Overall, the water-management results show that the optimised CA/HNT membrane combines water uptake, moisture retention, and vapour permeability, supporting its use as a candidate wound-contact material. Clinical suitability, however, cannot be concluded from WVTR alone and will depend on mechanical performance, exudate handling, sterilisation, and *in vivo* evaluation.

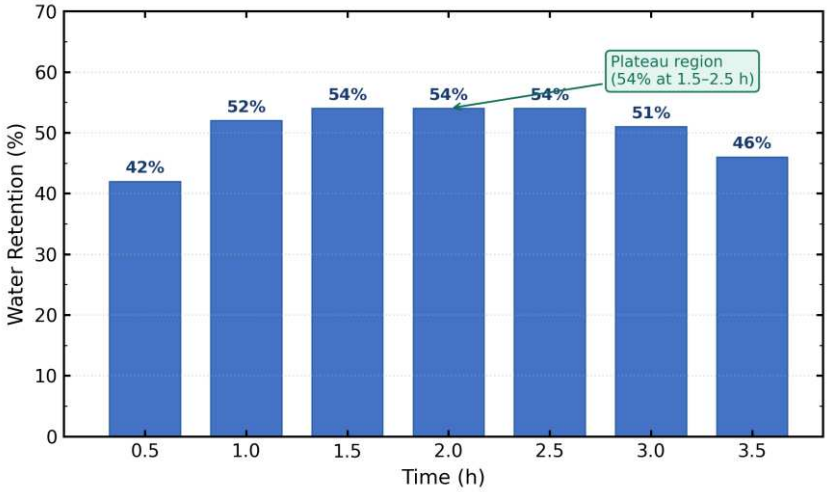


Fig. 5 Water retention of the CA/HNT/*S. junceum* nanofiber wound dressing (0.5–3.5 h). Plateau of 54% at 1.5–2.5 h

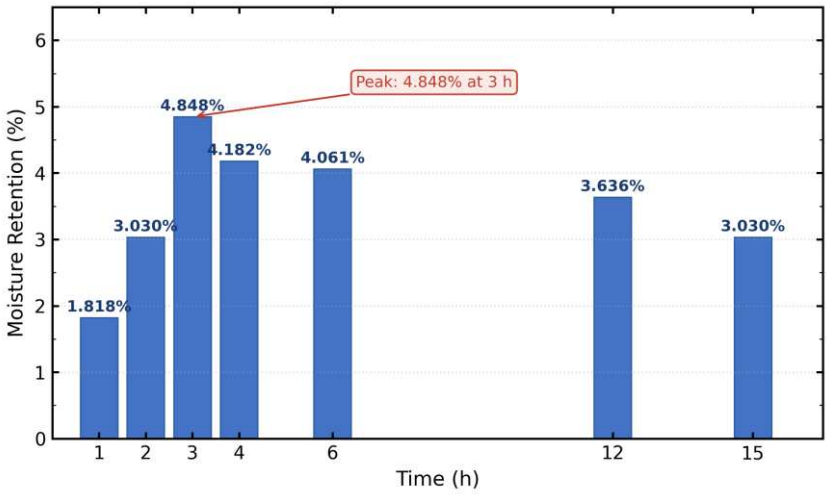


Fig. 6 Moisture retention of the CA/HNT/*S. junceum* nanofiber wound dressing (1–15 h). Peak of 4.848% at 3 h

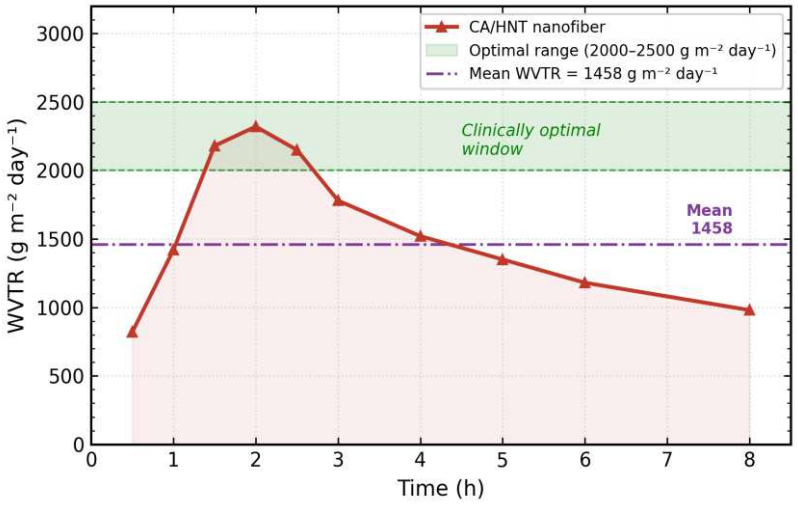


Fig. 7 Time-dependent WVTR of the CA/HNT/*S. junceum* nanofibrous dressing measured by ASTM E96-90 Procedure D at 35 °C. The dashed horizontal line indicates the overall mean (1458 g m−2 day−1); shaded literature ranges should be interpreted as contextual rather than universal clinical thresholds

3.6. In Vitro Biocompatibility

Biocompatibility measurements were obtained from three independent replicates (n = 3), with the underlying viability values provided in the Supporting Information (Table S1). Untreated control cultures displayed the characteristic elongated, spindle-shaped morphology of a healthy, proliferating L929 monolayer (Fig. 8). Across the tested extract-equivalent concentrations (0.78–50 µg mL−1) and incubation periods, metabolic activity remained above the 70% viability threshold specified in ISO 10993-5, supporting classification of the tested material/extract condition as non-cytotoxic (ISO 10993-5 2009); values at or above the untreated control indicate preserved metabolic activity but should not, by themselves, be read as direct evidence of cell proliferation.

The 72 h MTT results (Fig. 9) showed no concentration-dependent loss of viability across the tested range, and several conditions gave mean values slightly above the untreated control. Because MTT measures metabolic reduction rather than cell number directly, these increases are described as enhanced metabolic activity rather than definitive proliferation. Comparable cytocompatibility has been reported for other electrospun CA-containing wound-dressing systems (Dos Santos et al. 2021; Prakash et al. 2021; Samadian et al. 2020; Sharaf et al. 2022).

This cytocompatibility is consistent with the established use of CA as a biomedical polymer and with reports of acceptable cellular responses to halloysite-containing systems (Cao et al. 2020; Satish et al. 2019). The present experiment evaluates the complete material/extract condition and does not resolve the separate contributions of CA, HNT, and individual phytochemicals to L929 metabolic activity.

Overall, the MTT data show that the CA/HNT/*S. junceum* formulation was non-cytotoxic to L929 fibroblasts under the tested conditions. This finding provides the biological-safety basis for interpreting the scratch-migration assay that follows but does not, by itself, establish therapeutic wound-healing efficacy.

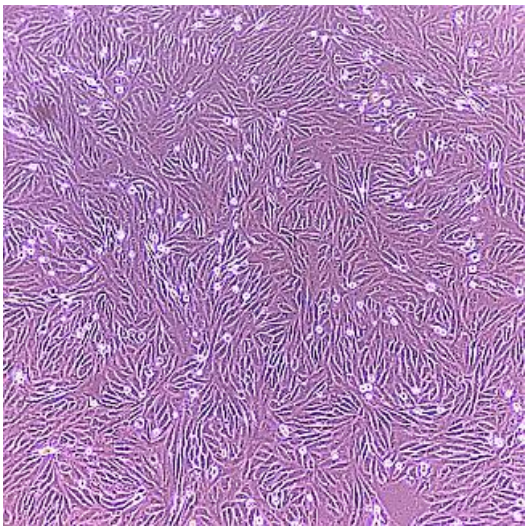


Fig. 8 L929 mouse fibroblast cells: characteristic spindle morphology of a healthy proliferating monolayer (untreated control)

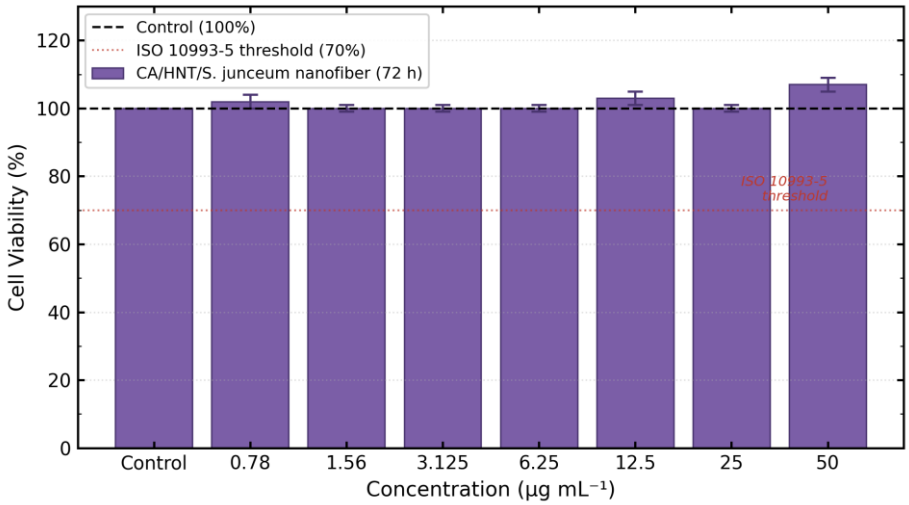


Fig. 9 L929 metabolic activity after exposure to the CA/HNT/*S. junceum* nanofiber condition for 72 h (MTT assay, n = 3, mean ± SD). Dashed line: untreated control (100%); dotted line: ISO 10993-5 cytotoxicity threshold (70%)

3.7. Wound Healing Scratch Assay

Representative scratch-assay images (Fig. 10) showed greater narrowing of the cell-free region in nanofiber-treated cultures than in untreated controls. Initial scratch widths were comparable at 0 h, and the difference became pronounced at 24 and 48 h, consistent with increased fibroblast migration under the tested conditions.

ImageJ analysis (Fig. 11) supported the microscopy observations: wound closure reached 77.5% in the treated group versus 24.8% in the untreated control at 24 h, and 97.2% versus 64.8% at 48 h. At 48 h, residual wound area was 2.78% in treated cultures versus 35.2% in controls ($p < 0.001$, two-tailed Student's t-test, n = 3; Section 2.10); the 24 h difference is descriptive and was not formally tested. These results demonstrate a strong pro-migratory effect in this L929 scratch model, though direct numerical comparison with other published dressing systems should be made cautiously, since cell type, extract preparation, dose, scratch geometry, and image-analysis procedures differ across studies (Samadian et al. 2020).

This migration result is compatible with the preserved metabolic activity observed in the MTT assay: the treatment did not reduce cell viability and was associated with faster closure of the artificial cell-free area. The assay does not, however, identify the molecular mechanism responsible for migration, and cannot establish that any individual GC–MS constituent caused the response.

Together, the MTT and scratch-assay data indicate cytocompatibility and enhanced fibroblast migration *in vitro*. These outcomes support further evaluation of the nanofibrous material as a wound-dressing candidate, while confirming regenerative efficacy will require mechanistic studies and *in vivo* wound models.

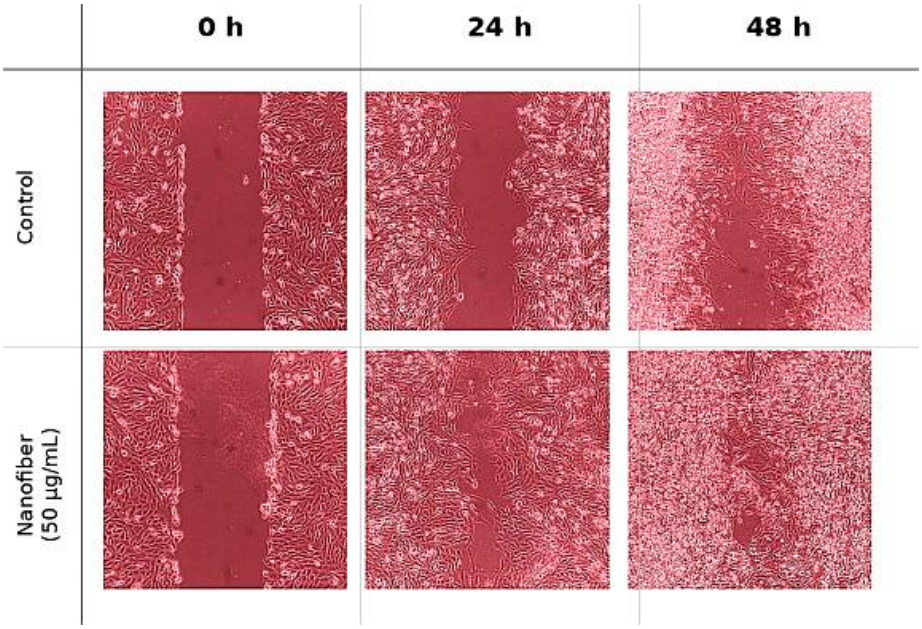


Fig. 10 Wound healing scratch assay: L929 fibroblast monolayer at 0, 24, and 48 h for untreated control and nanofiber-treated (50 µg mL⁻¹) groups

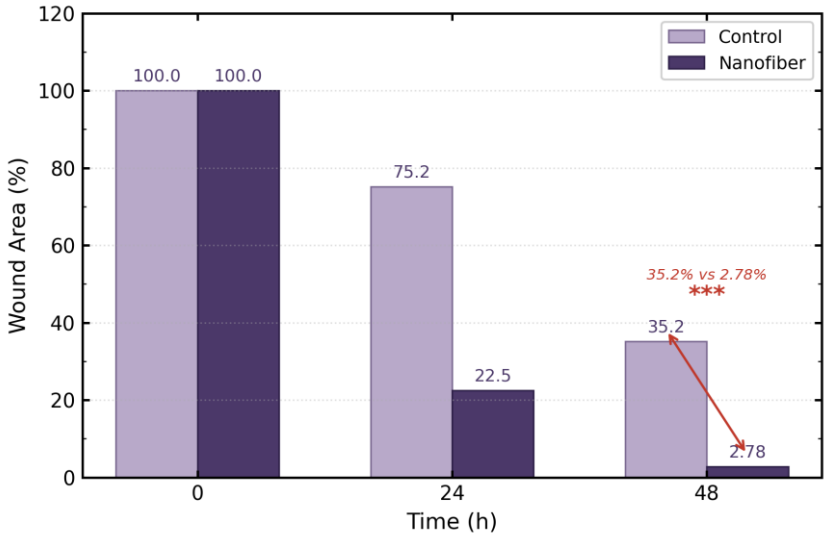


Fig. 11 Quantitative scratch-closure analysis at 0, 24, and 48 h (n = 3). At 48 h, ***p < 0.001 by Student's t-test. Scratch areas were quantified using ImageJ

3.8. Antioxidant capacity of release media

Antioxidant capacity of release media collected from the CA/HNT/*S. junceum* dressing was evaluated by the CUPRAC assay (Table 6). Total antioxidant capacity (TAC) increased from 0.038 mM Trolox equivalents at 0.5 h to a maximum of 0.055 mM at 2 h and remained measurable at 48 h (0.036 mM). Because separate specimens were analysed at each time point and CUPRAC measures reducing/antioxidant capacity rather than the concentration of a specific released molecule, these data describe time-dependent antioxidant availability rather than a cumulative drug-release profile, and do not by themselves establish a diffusion-controlled release mechanism (Apak et al. 2004).

The blank CA/HNT material showed only 0–0.002 mM Trolox equivalents over the same period, whereas the extract-loaded material gave substantially higher values (each analysis performed in triplicate), indicating that the

measured antioxidant capacity originated predominantly from the incorporated *S. junceum* fraction rather than from the unmodified CA/HNT matrix.

Antioxidant availability is relevant to wound-material design because excessive oxidative stress can impair cell and tissue repair (Comino-Sanz et al. 2021); however, the present data do not establish a causal link between CUPRAC values and the scratch-assay response. Confirming such a mechanism would require additional experiments — for example direct ROS measurements, identification/quantification of released compounds, or pathway-specific cellular assays.

Overall, the CUPRAC results show that antioxidant activity associated with the incorporated plant fraction remains detectable in the surrounding medium for up to 48 h. Together with cytocompatibility and enhanced fibroblast migration, this finding supports the functional potential of the material, without over-interpreting the CUPRAC assay as a complete release-kinetics study.

Table 6 Total antioxidant capacity (mM Trolox equivalents) measured in release media from extract-loaded and blank CA/HNT dressings (n = 3 per time point)

Sample	**0.5 h**	**1 h**	**2 h**	**3 h**	**4 h**	**8 h**	**12 h**	**24 h**	**48 h**
CA/HNT + Extract	0.038	0.048	0.055	0.052	0.051	0.035	0.039	0.038	0.036
CA/HNT (blank)	0.000	0.000	0.000	0.002	0.002	0.002	0.002	0.002	0.002

4. Conclusion

This study demonstrates an integrated cascade-valorisation route in which extractable fractions are recovered from *S. junceum* flowers before the residual lignocellulosic biomass is converted into cellulose acetate for electrospun wound-dressing fabrication, linking phytochemical recovery with cellulose-derivative production rather than treating these biomass fractions as independent resources.

The resulting cellulose acetate had a DS of 2.66 ± 0.04 and was successfully electrospun with extract-loaded HNT into a homogeneous nanofibrous formulation with fiber diameters of approximately 130–200 nm. FTIR, XRD, and DSC confirmed successful acetylation and described the structural and thermal characteristics of the polymer, while water-retention, moisture-retention, and WVTR measurements demonstrated functional water-management behaviour relevant to wound-contact materials.

Biologically, the formulation was non-cytotoxic to L929 fibroblasts under the tested conditions and increased scratch closure to 97.2% at 48 h versus 64.8% in untreated controls. CUPRAC analysis showed antioxidant activity in the release medium for up to 48 h, peaking at 2 h. These results support sustained antioxidant availability from the extract-containing material but do not, by themselves, establish compound-specific release kinetics or the molecular mechanism underlying the migration response.

Overall, *S. junceum* is shown to be a viable renewable feedstock for coupling cellulose-acetate production with recovery of extractable plant fractions in a single, materials-oriented workflow. These findings justify further development of the platform — particularly quantitative chemical release profiling, antibacterial testing, mechanical and sterilisation studies, and *in vivo* wound-healing evaluation. A complete mass balance and environmental assessment would also be required before the process could be described quantitatively as zero-waste or environmentally superior at scale.

References

Affonso RCL, Voytena APL, Fanan S, Pitz H, Coelho DS, Horstmann AL, Pereira A, Uarrota VG, Hillmann MC, Varela LAC, Ribeiro-do-Valle RM, Maraschin M (2016) Phytochemical composition, antioxidant activity, and the effect of the aqueous extract of coffee (Coffea arabica L.) bean residual press cake on the skin wound healing. Oxid Med Cell Longev 2016:1923754. https://doi.org/10.1155/2016/1923754

Angelini LG, Lazzeri A, Levita G, Fontanelli D, Bozzi C (2000) Ramie (Boehmeria nivea (L.) Gaud.) and Spanish broom (*Spartium junceum* L.) fibres for composite materials: agronomical aspects, morphology and mechanical properties. Ind Crops Prod 11:145–161. https://doi.org/10.1016/S0926-6690(99)00059-X

Apak R, Güçlü K, Özyürek M, Karademir SE (2004) Novel total antioxidant capacity index for dietary polyphenols and vitamins C and E, using their cupric ion reducing capability in the presence of neocuproine: CUPRAC method. J Agric Food Chem 52:7970–7981. https://doi.org/10.1021/jf048741x

Boateng JS, Matthews KH, Stevens HNE, Eccleston GM (2008) Wound healing dressings and drug delivery systems: a review. J Pharm Sci 97:2892–2923. https://doi.org/10.1002/jps.21210

Candido RG, Gonçalves AR (2016) Synthesis of cellulose acetate and carboxymethylcellulose from sugarcane straw. Carbohydr Polym 152:679–686. https://doi.org/10.1016/j.carbpol.2016.07.071

Cansado IPP, Mourão PAM, Castanheiro JE, Geraldo PF, Suhas, Suero SR, Cano BL (2025) A review of the biomass valorization hierarchy. Sustainability 17:335. https://doi.org/10.3390/su17010335

Cao X, Liu H, Yang X, Tian J, Luo B, Liu M (2020) Halloysite nanotubes@polydopamine reinforced polyacrylamide-gelatin hydrogels with NIR light triggered shape memory and self-healing capability. Compos Sci Technol 191:108071 **[DOI to verify]**

Cardoso CRB, Souza MA, Ferro EAV, Favoreto S Jr, Pena JDO (2004) Influence of topical administration of n-3 and n-6 fatty acids on the healing of cutaneous wounds. Wound Repair Regen 12:235–243. https://doi.org/10.1111/j.1067-1927.2004.012216.x

Cerchiara T, Straface SV, Chidichimo G, Belsito EL, Liguori A, Luppi B, Bigucci F, Zecchi V (2012) *Spartium junceum* aromatic water: chemical composition and antitumor activity. Nat Prod Commun 7:137–140. https://doi.org/10.1177/1934578X1200700143

Cerqueira DA, Rodrigues Filho G, Meireles CS (2007) Optimization of sugarcane bagasse cellulose acetylation. Carbohydr Polym 69:579–582. https://doi.org/10.1016/j.carbpol.2007.01.010

Chen J, Xu J, Wang K, Cao X, Sun R (2016) Cellulose acetate fibers prepared from different raw materials with rapid synthesis method. Carbohydr Polym 137:685–692. https://doi.org/10.1016/j.carbpol.2015.11.034

Comino-Sanz IM, López-Franco MD, Castro B, Pancorbo-Hidalgo PL (2021) The role of antioxidants on wound healing: a review of the current evidence. J Clin Med 10:3558. https://doi.org/10.3390/jcm10163558

Das AM, Ali AA, Hazarika MP (2014) Synthesis and characterization of cellulose acetate from rice husk: eco-friendly condition. Carbohydr Polym 112:342–349. https://doi.org/10.1016/j.carbpol.2014.06.006

Dhivya S, Padma VV, Santhini E (2015) Wound dressings – a review. BioMedicine 5:22 https://doi.org/10.7603/s40681-015-0022-9

Dilika F, Bremner PD, Meyer JJM (2000) Antibacterial activity of linoleic and oleic acids isolated from Helichrysum pedunculatum: a plant used during circumcision rites. Fitoterapia 71:450–452

Djuned FM, Asad M, Mohamad Ibrahim MN, Wan Daud WR (2014) Synthesis and characterization of cellulose acetate from TCF oil palm empty fruit bunch pulp. BioResources 9:4710–4721. https://doi.org/10.15376/biores.9.3.4710-4721

Dos Santos AEA, Dos Santos FV, Freitas KM, Pimenta LPS, de Oliveira Andrade L, Marinho TA, de Avelar GF, da Silva AB, Ferreira RV (2021) Cellulose acetate nanofibers loaded with crude annatto extract: preparation, characterization, and in vivo evaluation for potential wound healing applications. Mater Sci Eng C 118:111322. https://doi.org/10.1016/j.msec.2020.111322

Edgar KJ, Buchanan CM, Debenham JS, Rundquist PA, Seiler BD, Shelton MC, Tindall D (2001) Advances in cellulose ester performance and application. Prog Polym Sci 26:1605–1688

Fakhrullin RF, Lvov YM (2016) Halloysite clay nanotubes: a multifunctional platform for the intracellular delivery of drugs and nucleic acids. Nanomedicine 11:2243–2246 **[DOI to verify]**

French AD (2014) Idealized powder diffraction patterns for cellulose polymorphs. Cellulose 21:885–896. https://doi.org/10.1007/s10570-013-0030-4

Haider A, Haider S, Kang IK (2018) A comprehensive review summarizing the effect of electrospinning parameters and potential applications of nanofibers in biomedical and biotechnology. Arab J Chem 11:1165–1188

ISO (2009) ISO 10993-5:2009 Biological evaluation of medical devices—Part 5: Tests for in vitro cytotoxicity. International Organization for Standardization, Geneva

Jangde R, Srivastava S, Singh MR, Singh D (2018) In vitro and in vivo characterization of quercetin loaded multiphase hydrogel for wound healing application. Int J Biol Macromol 115:1211–1217

Johnson M, Abugri DA (2014) Occurrence, biochemical, antimicrobial and health effects of palmitic acid. In: Porto LF (ed) Palmitic acid. Nova Science Publishers, New York, pp 17–44

Jones V, Grey JE, Harding KG (2006) Wound dressings. BMJ 332:777–780. https://doi.org/10.1136/bmj.332.7544.777

Junker JPE, Kamel RA, Caterson EJ, Eriksson E (2013) Clinical impact upon wound healing and inflammation in moist, wet, and dry environments. Adv Wound Care 2:348–356 https://doi.org/10.1089/wound.2012.0412

Karaboyaci Ö, Kılıç S (2022) Cellulose acetate production and characterization from *Spartium junceum*. Fresenius Environ Bull 31:7529–7534

Katović D, Katović A, Krnčević M (2011) Spanish broom (*Spartium junceum* L.)—history and perspective. J Nat Fibers 8:81–98. https://doi.org/10.1080/15440478.2011.577277

Kovačević Z, Sutlović A, Matin A, Bischof S (2021) Natural dyeing of cellulose and protein fibers with the flower extract of *Spartium junceum* L. plant. Materials 14:4091. https://doi.org/10.3390/ma14154091

Kürschner K, Hoffer A (1931) A new quantitative cellulose determination. Chem Ztg 55:161

Li D, Xia Y (2004) Electrospinning of nanofibers: reinventing the wheel? Adv Mater 16:1151–1170 https://doi.org/10.1002/adma.200400719

Liu Q, Luo S, Peng J, Chang R (2024) Electrospun nanofibers from plant natural products: a new approach toward efficient wound healing. Int J Nanomedicine 19:13973–14002

Lvov Y, Wang W, Zhang L, Fakhrullin R (2016) Halloysite clay nanotubes for loading and sustained release of functional compounds. Adv Mater 28:1227–1250 https://doi.org/10.1002/adma.201502341

Martins Vilas-Boas A, Campos DA, Pintado MM (2025) Valorization of food by-products for bio-based hydrogel development. Food Rev Int 41:3589–3615

Mujtaba M, Fraceto LF, Fazeli M, Mukherjee S, Savassa SM, de Medeiros GA, Pereira AES, Mancini SD, Lipponen J, Vilaplana F (2023) Lignocellulosic biomass from agricultural waste to the circular economy: a review with focus on biofuels, biocomposites and bioplastics. J Clean Prod 402:136815. https://doi.org/10.1016/j.jclepro.2023.136815

Nanni V, Canuti L, Gismondi A, Canini A (2018) Hydroalcoholic extract of *Spartium junceum* L. flowers inhibits growth and melanogenesis in B16-F10 cells by inducing senescence. Phytomedicine 46:1–10. https://doi.org/10.1016/j.phymed.2018.06.008

Nishikawa M, Nojima M, Akiyama T, Sankawa U, Iitaka K (1976) Antitumor activity of myristic acid against solid tumors in mice. Gann 67:951–957

Pham QP, Sharma U, Mikos AG (2006) Electrospinning of polymeric nanofibers for tissue engineering applications: a review. Tissue Eng 12:1197–1211 https://doi.org/10.1089/ten.2006.12.1197

Prakash J, Venkataprasanna KS, Bharath G, Banat F, Niranjan R, Venkatasubbu GD (2021) In-vitro evaluation of electrospun cellulose acetate nanofiber containing graphene oxide/TiO2/curcumin for wound healing application. Colloids Surf A Physicochem Eng Asp 627:127166. https://doi.org/10.1016/j.colsurfa.2021.127166

Prinz Setter O, Segal E (2020) Halloysite nanotubes—the nano-bio interface. Nanoscale 12:23444–23460. https://doi.org/10.1039/D0NR06820A

Rodrigues Filho G, Monteiro DS, da Silva Meireles C, de Assunção RMN, Cerqueira DA, Barud HS, Ribeiro SJL, Messaddeq Y (2008) Synthesis and characterization of cellulose acetate produced from recycled newspaper. Carbohydr Polym 73:74–82. https://doi.org/10.1016/j.carbpol.2007.11.010

Samadian H, Zamiri S, Ehterami A (2020) Electrospun cellulose acetate/gelatin nanofibrous wound dressing containing berberine for diabetic foot ulcer healing. Sci Rep 10:8312

Satish S, Tharmavaram M, Rawtani D (2019) Halloysite nanotubes as a nature's boon for biomedical applications. Nanobiomedicine 6:1–16. https://doi.org/10.1177/1849543519863625

Sharaf SS, El-Shafei AM, Refaie R, Gibriel AA, Abdel-Sattar R (2022) Antibacterial and wound healing properties of cellulose acetate electrospun nanofibers loaded with bioactive glass nanoparticles: in-vivo study. Cellulose 29:4565–4577. https://doi.org/10.1007/s10570-022-04570-1

Silva JR, Burger B, Kühl CM, Candreva T, Dos Anjos MB, Rodrigues HG (2018) Wound healing and omega-6 fatty acids: from inflammation to repair. Mediators Inflamm 2018:2503950. https://doi.org/10.1155/2018/2503950

Xue J, Wu T, Dai Y, Xia Y (2019) Electrospinning and electrospun nanofibers: methods, materials, and applications. Chem Rev 119:5298–5415

Xue J, Xie J, Liu W, Xia Y (2017) Electrospun nanofibers: new concepts, materials, and applications. Acc Chem Res 50:1976–1987 https://doi.org/10.1021/acs.accounts.7b00218

Zahreddine H, Hijazi A, Rammal H (2021) Chemical composition and antioxidant capacity of *Spartium junceum* grown in Lebanon. J Med Res Health Sci 4:1588–1591. https://doi.org/10.52845/JMRHS/2021-4-11-10

Statements and Declarations

Funding

This work was supported by Süleyman Demirel University Scientific Research Projects Unit (Project No. 8081).

Competing interests

The authors have no relevant financial or non-financial interests to disclose.

Author contributions

Özlem Yılmaz Karaboyacı: conceptualisation, methodology, investigation, data curation, writing—original draft, writing—review and editing. Semra Kılıç: supervision, writing—review and editing. Both authors read and approved the final manuscript.

Data availability

The data that support the findings of this study are available from the corresponding author upon reasonable request. Mean MTT viability values and ImageJ-derived scratch-closure measurements are provided in the Supporting Information (Tables S1–S2).

Ethics approval

Not applicable. The study used the established L929 cell line and did not involve human participants or experimental animals.

Consent to participate

Not applicable.

Consent for publication

All authors approved the manuscript for publication.

Supplementary information

Supplementary information (Tables S1–S2) includes mean MTT viability values and ImageJ-derived scratch-closure measurements referenced in the main text.

Supplementary Files

This is a list of supplementary files associated with this preprint. Click to download.

- SpartiumjunceumSupplementaryInformationCellulose.docx